---

**Article:**
Contreras-Arratia, R and Neuberg, JW orcid.org/0000-0001-7866-0736 (2020) Towards reconciling seismic and geodetic moment estimations: Case Bárðarbunga. Journal of Volcanology and Geothermal Research, 408. 107034. ISSN 0377-0273

https://doi.org/10.1016/j.jvolgeores.2020.107034

---

# Towards reconciling seismic and geodetic moment estimations: Case Bárðarbunga

**Rodrigo Contreras-Arratia* and Jurgen W Neuberg**

*Institute of Geophysics and Tectonics, School of Earth and Environment, University of Leeds, Leeds LS2 9JT, UK*

* Corresponding author at: Institute of Geophysics and Tectonics, School of Earth and Environment, University of Leeds, Leeds LS2 9JT, UK.

E-mail addresses: r.contreras.arratia@gmail.com (R. Contreras-Arratia), j.neuberg@leeds.ac.uk (J. Neuberg)

## Abstract

Previous studies have found discrepancies concerning the seismic radiation between planar and curved faults: moment tensor (MT) interpretations, seismic moment estimation and waveforms change dramatically when the rupture is not planar. Therefore, assuming a point source on a planar fault for earthquakes in volcanic environments can be an oversimplification that needs to be addressed if we observe some seismological clues. We study MT inversions for the biggest earthquakes during the 2014-2015 collapse of the Bárðarbunga caldera, which show non-double couple solutions, with vertical compression axis. We calculate synthetic seismograms for partial-ring ruptures using an ideal seismic network, and one emulating the existing monitoring network at Bárðarbunga. Observations using distal stations can return a better-constrained seismic moment, but they fail to characterise the dynamics involved. On the other hand, using proximal stations we obtain a reliable representation of the forces involved. However, the seismic moment is systematically overestimated due to the proximity to the curved source and the corresponding focusing effects. Finally, we correct the area of rupture due to fault shape to estimate the real cumulative seismic moment during the caldera collapse. The result shows a closer relationship between seismic and geodetic moment. In particular, both estimations match when we use a realistic rigidity for a volcanic environment.

## 1. Introduction

The energy released by an earthquake is given by the seismic moment ($M_o$) which for a planar fault is linearly dependent on the average slip on the fault ($\overline{D}$), the rupture area ($A$) and the shear modulus of the surrounding rock ($\mu$) (Aki and Richards, 2002). If the rupture area is small compared to the wavelength the earthquake can be considered as taking place in a point in space i.e. point source. However, as the area increases, the approximation is no longer valid and the description of the earthquake needs a representation of the rupture area as the superposition of several point sources (extended fault model). In this study, we focus on a special case of rupture, ring faults, with caldera-size dimensions with diameters of about 5 km.

We apply the ring-fault model proposed by Contreras-Arratia and Neuberg (2019) to the Bárðarbunga caldera collapse, explaining more accurately the geometrical problem, moment tensor (MT) inversions and seismic moment estimation. It is evident that the Bárðarbunga caldera as a whole

is formed by a non-perfect ring fault. For small events, the curvature of the rupture area is negligible and therefore can be explained by a single double couple (DC) (Ágústsdóttir et al., 2019), on the other hand, for bigger ruptures, the curvature comes into play and a more complex model is needed to explain the observations. Moreover, MT solutions reported for these events (Riel et al., 2015; Gudmundsson et al., 2016) include an important Compensated Linear Vector Dipole (CLVD) component, which Ekström (1994) attributed to outward dipping ring-fault ruptures. Thus, these MT solutions are a good indicator that curved-ruptures are applicable.

Previous results on the 2014 Bárðarbunga caldera collapse support the idea of an aseismic collapse (Riel et al., 2015), which implies creeping slip at the caldera rims or a tremor-like superposition of events forming a slow slip event. These processes are very likely to occur, therefore, there is always a discrepancy when comparing seismic and geodetic moment. Here we propose that the partial wave interference produced by the radiation of different point sources plays an additional role in being responsible for the low value of the seismic moment. By applying the ring-fault model we re-calculate the areas of rupture for each event and determine the cumulative seismic moment, which can then be compared to the geodetic moment.

### *1.1. Ring faults: conduits*

We showed previously (Contreras-Arratia and Neuberg, 2019), that partial- or full-ring ruptures, with a radius of tens of meters (conduits), cannot be directly represented by a single-source model. The planar geometry of a classic point source produces the highest amplitudes, however, increasing the fault curvature while keeping the rupture area constant result in decreasing amplitudes. Thus, if we assume a planar seismic source instead of the real curved source, the seismic moment is systematically underestimated. Moreover, the waveforms produced by opposed double couples at close proximity (dyke and full-ring) are the time derivative of the waveform predicted by the source theory in the far-field. This implies that if we assume a planar fault framework, an MT inversion returns the derivative of the actual slip history. Finally, the MT solutions for these curved sources return dominant CLVD and isotropic (ISO) components, which points to a reorganisation or change of volume, respectively, regardless of the pure shear nature (DC) of the ruptures.

Ekström (1994) studied the MT components produced by outward-dipping ring faults after the isotropic component was set to zero, he found a trade-off between DC and CLVD components while varying the dipping angle. Nettles and Ekström (1998); Shuler and Ekström (2009); Shuler et al. (2013b,a) reported vertical- and sub-vertical-CLVD focal mechanisms at Bárðarbunga, Nyiragongo, Rabaul, Tungurahua, Miyakejima, among others. These results were explained by ring fault rupture models. Shuler et al. (2013a) proposed the inclusion of the isotropic component in the analysis, they consider a trade-off between isotropic and CLVD, alongside with smaller DC contribution, which can be a more appropriate description. In this study, we use the classic decomposition of the moment tensor to be a summation of the ISO, CLVD and DC components. The isotropic component represents homogeneous tension or pressure forces, i.e. explosion and implosion, respectively. The sum of all components (ISO, DC and CLVD) represents the 100% of the seismic moment.

### *1.2. Caldera collapse: Bárðarbunga, 2014-2015*

The Bárðarbunga caldera is located in central Iceland under a tensional stress regime due to divergent Eurasia and North American plates. Gravity studies (Gudmundsson and Högnadóttir, 2007) have shown that its roof aspect ratio is fairly low (height/width $= 5/11 \sim 0.5$), i.e. the caldera roof is thin and wide, this is also supported by Ágústsdóttir et al. (2019) who located the fragile-ductile transition at $6-7$ km depth. During a caldera collapse of these characteristics, special fault

systems develop (Roche et al., 2000). Acocella (2007) defined stages to explain this kind of caldera formation process, according to experiments, calderas evolve from an initial downsag type (stage 1) collapse showing no seismicity followed by thrust faults developed at the boundaries (stage 2), later, a combination of the two previous stages is developed (stage 3) and finally, normal faults are created outside the pre-existing reverse faults (stage 4). Previous studies of the seismicity at Bárðarbunga showed tensional, vertical CLVD focal mechanisms supporting the conceptual model at stage 2 of caldera formation (Nettles and Ekström, 1998; Tkalčić et al., 2009).

Riel et al. (2015); Gudmundsson et al. (2016); Ágústsdóttir et al. (2019) studied seismicity during the 2014-2015 collapse which was concentrated at both the north-northwest and southern parts of the caldera. In summary, the seismicity was interpreted as normal DC solutions for small events ($M_w > 4.5$), whereas for bigger events, non-DC component (CLVD and ISO) become dominant (Rodriguez Cardozo et al., 2018). Most focal mechanisms show vertical pressure axes (stage 4, normal faulting according to Acocella (2007)) and can be explained by inner dipping normal ring-faults. Gudmundsson et al. (2016) calculated the cumulative seismic moment for the whole caldera collapse process as $M_o = 5.07 \times 10^{18}$ Nm, and the geodetic moment $M_o^{(g)}$ in the range of $4 \times 10^{19}$ Nm for a rigidity of $\mu = 2$ GPa and $4 \times 10^{20}$ Nm for $\mu = 20$ GPa, assuming a total average slip at the ring-fault of 60 m and a vertical extent of the ring-fault of 12 km. Parks et al. (2017) have recalculated slip distribution at the boundaries of the caldera, finding an average slip of 40 m. Moreover, Ágústsdóttir et al. (2019) have localised the seismicity finding the fragile-ductile transition at 7 km depth, delimiting the bottom of the ring-fault, in contrast to the previous estimation (Gudmundsson et al., 2016).

## 2. Methodology

By analysing the reported features of seismicity at Bárðarbunga (Riel et al., 2015; Gudmundsson et al., 2016; Ágústsdóttir et al., 2019), we suspect that ring faults are activated due to the non-DC components reported. We create synthetic seismograms for partial- and full-ring ruptures using Specfem3D (Tromp et al., 2008). We represent curved fault surfaces by a superposition of single DC point sources with seismic moment $M_o = 4 \times 10^{20}$ Nm, following the methodology described in Contreras-Arratia and Neuberg (2019). Our study is divided into two parts, which are described as follows:

- In order to obtain MT components, we simulate extended partial-ring ruptures with a radius of $R = 3.5$ km and constant dip $= 60°$ for three different rake angles $\lambda = [-45°, -90°, -135°]$ (negative for normal faults). The strike varies from consecutive point sources in $10°$ increments, forming a 1/4-ring rupture centred at azimuth $-15°$. The duration of the slip function is 40 s, therefore P, S and near field phases arrive in one single wave package. We use two synthetic seismic networks to record these events, the first emulates the real Icelandic Meteorological Observatory (IMO) seismic network (Fig. 1a and b), and second, an ideal network covering sufficiently azimuth and take-off angles, the latter defined with respect to the vertical upward axis (Fig. 1c). The aim is to reproduce the MT solutions observed in nature (Riel et al., 2015; Rodriguez Cardozo et al., 2018) with our complex rupture models.

- In order to study how the magnitude of an event is affected by the curvature of the source we consider 1/4-, 1/2-, 3/4- and full-ring ruptures with radius $R = 3.5$ km, $60°$ dip and $-90°$ rake. The sources in all cases are separated by $5°$ angular arc, therefore, the ruptures are

represented by 18, 36, 54 and 72 sources, respectively. We calculate their seismic moments using the IMO network, which provides acceptable results for magnitude estimation. We compare them with the seismic moment of a single source multiplied by the number of point sources composing the ring-ruptures. The ratio of the seismic moment produced by a planar source divided by the seismic moment of the same-size curved fault ($M_o^P/M_o$) gives us a correction factor which can be applied to compensate for the underestimated rupture area, hence, seismic moment.

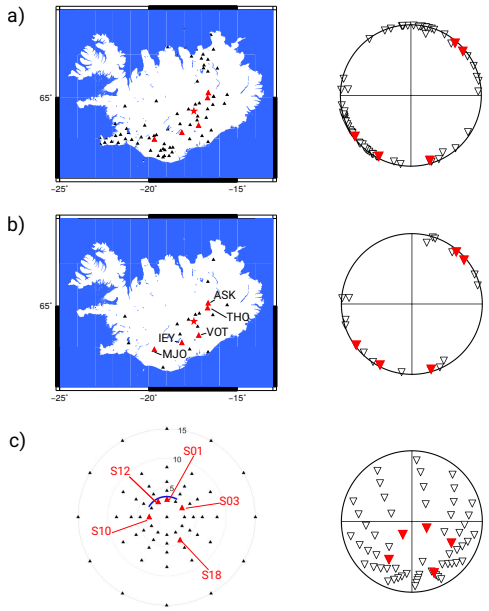


Figure 1: Station locations used for modelling. a) Icelandic Meteorological Office (IMO) stations and their locations on the focal sphere. b) Subset of IMO, actually used for modelling. c) Ideal network simulated, with stations up to 15 km away and a very good focal sphere coverage. Note the enhanced coverage with the Ideal network.

The period used for the slip function was selected to avoid errors during the inversion by satisfying the Fraunhofer diffraction condition (Aki and Richards, 2002), which ensures a stationary interference pattern. The shape of the extended-source waveform can be seriously deformed if the wavelength and therefore the period is not long enough. Shorter wavelengths are observed in nature and give important information about the dimensions of the source, however, for our analysis, we need to low-pass filter the signals in order to apply point source MT inversions. In this article we simplify the problem by using the same source time function for all the sources, however, they can be different in shapes and durations. We can perform the same study with different wavelengths only if the shortest wavelength satisfies the Fraunhofer diffraction condition.

The waveforms obtained from the forward modelling are subjected to MT inversions using the software package KIWI (Cesca et al., 2010). This returns the mathematical representation of the best DC solution and the full moment tensor, both based on a point source approach. No source time function is calculated. The Green's functions were created using the software package Fomosto with QSEIS backend (Heimann et al., 2019; Wang, 1999) and a Gaussian wavelet in a half-space

medium. The analysis of the moment tensors returned is based on the focal mechanisms showing information about the deviatoric MT, the seismic moment related to the magnitude, and the so-called lune plot which gives information of the full moment tensor (Tape and Tape, 2012).

The focal mechanisms provided by the KIWI software are based on the deviatoric components only (DC + CLVD) and indicate the polarisation on a focal sphere, which contains information about the principal axes for each source. In contrast, the lune plot shows the full moment tensor solution, where the deviatoric components are aligned at 0° latitude between the DC at the centre and CLVD at the edges (second row Fig. 2). The latitude position of the solution gives a measure of the importance of the ISO component (explosion at the top, implosion at the bottom). The focal mechanism dominated by isotropic components (white or black "beachball") cannot provide any information on the principal axes. The same is valid for the lune plot, which is only a map representation of the importance of each component of the moment tensor. Therefore, both representations, focal mechanisms and lune plots are complementary. In any case, we label the solutions as consistent if two conditions are satisfied: (i) the vertical forces for the CLVD and isotropic component must have the same sign and (ii) the deviatoric solution must be consistent with solutions for partial ring rupture proposed by Ekström (1994). The solutions which do not satisfy these conditions are labelled as biased due to artefacts introduced by the network configuration.

Finally, using the seismic moments calculated for different arc ruptures at Bárðarbunga, we estimate the correction factor for the seismic moment under the assumption of the respective partial-ring rupture. The underestimation of the seismic moment by assuming a planar fault can be important while comparing the cumulative seismic moment with the geodetic moment of the whole caldera collapse process. By definition, these quantities give information about the seismic energy radiated and the strain energy, only for planar faults, therefore, their direct application to ring faults can lead to misinterpretations.

## 3. Results: Bárðarbunga caldera collapse

In this section, we show the MT solutions and the seismic moment estimations for each case. The aim is to contrast information given by different synthetic seismic networks when we analyse a volcanic event similar to the ones that occurred at Bárðarbunga during 2014, regarding its dynamics and magnitudes. The results, described in the next two paragraphs, are obtained by using the seismic networks shown in Fig. 1b and 1c. The results of the inversion are shown in Fig. 2 and summarised in Table 1 and 2.

- Moment tensor estimations: The MT inversions show contradictory results when using these three different seismic networks. The ideal network shows a consistent superposition of DC, CLVD and ISO (mostly implosion, i.e. negative diagonal components of the MT) for all three rake angles (Table 1). By analysing the deviatoric component shown by the focal mechanisms in the first row of Fig. 2c, we observe that the pressure axis returned by the inversion software is consistent with previous studies (Ekström, 1994) and the directions of the slip vector. Moreover, considering that the individual faults modelled are normal (negative rake angles) the semi-vertical pressure axes are consistent with the dominant isotropic component (implosion) shown in the lune plots (second row in Fig. 2c). In contrast, the IMO network and its subset provide solutions which are not consistent with the theory postulated by Ekström (1994) i.e. rake angles are not compatible with pressure/tension axes in the focal mechanism solutions (first row in Fig. 2a and 2b). Furthermore, the lune plots (second row in Fig. 2a and

2b) show inconsistent results for the ISO component by only varying the rake angle, which is a clear artefact due to the station configuration and the absence of seismic stations in the proximity of the caldera. In other words, we should not expect such a dramatic change in the full moment tensor, only by changing the rake angle 45°. Finally, in Fig. 3, we show the match between the seismograms and the synthetics predicted by the source models for the three inversions and five stations each. For all the networks the fit appears to be very good, regardless of how different the source models are.

- Seismic moment $M_o$ estimations: The seismic moment estimations obtained by the two networks also show incompatible results. On one hand, the ideal network, which retrieves a good quality MT estimation, fails to provide a realistic seismic moment estimation, due to a concentration of energy inside the ring fault. All individual contributions to the radiation interfere constructively inside the ring, i.e. focusing effect (Contreras-Arratia and Neuberg, 2019), which is a direct result of the geometry and not of the seismic energy released by the earthquake. This can be observed in Fig. 4b, where the amplitude profiles for curved sources in red and black exhibit unusual larger amplitudes for proximal stations. When we compare these profiles with a point source profile (such as the shown in blue), lead to an overestimation of the seismic moment and therefore the magnitude of the event, i.e. the seismic moment needs to be very high to fit the red or black curves with a power-law such as the blue curve. Moreover, the fact that the ring fault and the point source used as hypocentre for the MT inversion are not at the same location (Fig. 4a) results in an increase of the misfits for all source parameter estimations. Nevertheless, the seismic moments obtained by the IMO network can be trusted, since for long epicentral distances the amplitude decay is similar for a point source and a ring source, reducing the effect of the geometry in the seismic moment estimation. In summary, we calculate the seismic moment by using seismograms from stations at long epicentral distances, thus, the complex fault can be seen as a point source.

- The seismic moments calculated for different partial ruptures with rake $= -90°$ in a caldera-size ring are shown in Table 2. The ratio between the seismic moment of a planar rupture and the seismic moment of the same area but curved $M_o^P/M_o$, gives us the value needed to correct the seismic moment returned by the inversion. Thus, we can obtain a seismic moment which accurately estimates the real rupture area. In all cases the ratio is bigger than one, therefore, the apparent seismic moment increases. In our previous study, we obtained correction factors for conduit-size ring-faults in the range of 1.1 for a 1/4-ring to 42 for a full-ring rupture (Contreras-Arratia and Neuberg, 2019). For caldera-size ring-faults, we obtain correction factor in the range 2.9 to 9.7, respectively (Table 2). If we assume that all events in a caldera-size fault are 1/4-ring ruptures, the cumulative seismic moment for planar faults needs to be multiplied by 2.9 to obtain the seismic moment with the real rupture area. On the other hand, if we assume only full-ring ruptures, the correction approaches one order of magnitude. The corrections for ring ruptures follows the same principle, the source magnitude is underestimated. However, correction factors for conduit-size and caldera-size are dramatically different, hence, the application of this conceptual model for different ring sizes needs to be modelled for each particular case.

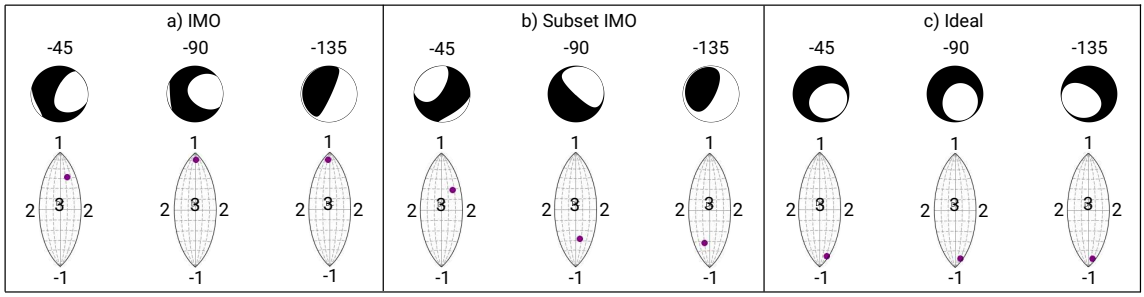


Figure 2: Analysis of the results provided by inversion software: Focal mechanisms showing the deviatoric components of the MT solution and lune plots showing the full MT solution (dark dots). Three 1/4-ring ruptures with 60° dip and different rake angles were analysed ($\lambda = [-45°, -90°, -135°]$). For lune plots, 1: Explosion (positive isotropic component: tensional forces), -1: Implosion (negative isotropic component: pressure forces), 2: CLVD and 3: DC.

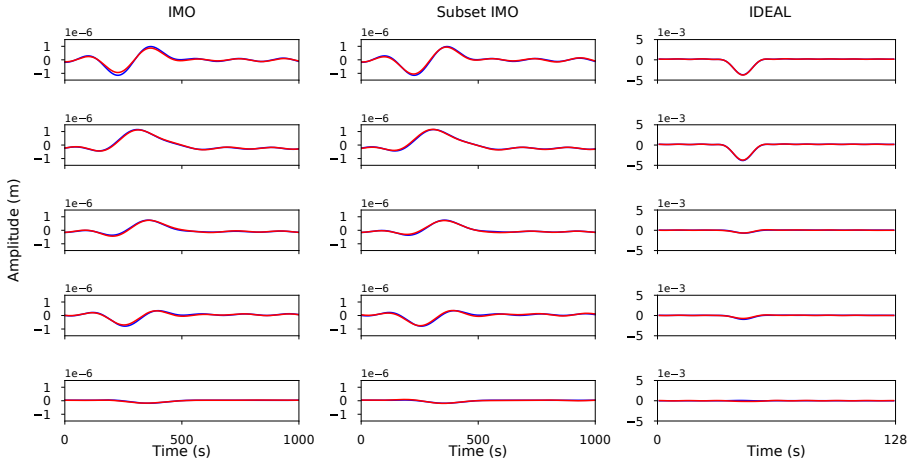


Figure 3: Examples of waveform match between input seismograms (blue) and synthetics produced by the inversion software (red). The match is very good for the three inversions and all the stations. (Left) For the source inverted using the IMO network, we show waveforms from station VOT, THO, ASK, IEY and MJO (Fig. 1b). (Centre) For the source inverted using the subset of IMO stations, we show waveforms from the same previous stations. (Right) For the ideal network, we show waveforms from the stations S01, S13, S03, S10 and S18 (Fig. 1c). Note that the fit appears to be very good regardless of the type of the source model returned. For the first two cases, we used a lowpass filter of 0.005 Hz corner frequency. For the last case, a lowpass filter with 0.08 Hz corner frequency. Note that the time scales are different. For interpretation of the colour scales in this figure, the reader is referred to the online version of this article.

## 4. Discussion

In our previous study (Contreras-Arratia and Neuberg, 2019), we showed that classical methods for inversion of seismic sources cannot be directly applied to non-planar ruptures since problems arise when the shape of the fault is oversimplified. However, understanding the link between these complex sources and the results given by different software packages is of major importance, since we can quantify the uncertainties in moment tensor inversions and apply corrections. Furthermore,

| Source | Rake | DC % | CLVD % | ISO % | $M_o$ IMO network | $M_o$ ideal network |
|---|---|---|---|---|---|---|
| 1/4-ring | $-45°$ | 8 | 32 | 60 | $3.87 \times 10^{14}$ Nm | $3.00 \times 10^{15}$ Nm |
| 1/4-ring | $-90°$ | 7 | 28 | 65 | $5.73 \times 10^{14}$ Nm | $1.14 \times 10^{15}$ Nm |
| 1/4-ring | $-135°$ | 15 | 20 | 65 | $5.36 \times 10^{14}$ Nm | $1.23 \times 10^{15}$ Nm |

Table 1: MT solutions for three 1/4-ring ruptures with different rake values in a caldera-size ring-fault using the ideal network. Also, their magnitude estimation using the subset of IMO and ideal networks, these networks are shown in Fig. 1b and c.

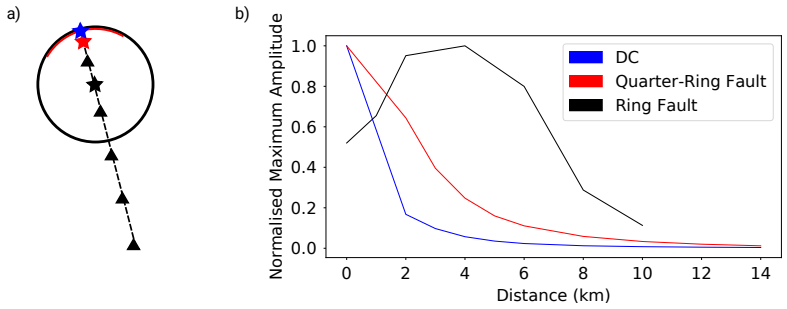


Figure 4: Maximum amplitude as a function of the epicentral distance for different faults. a) Scheme showing 3 ruptures: point source DC (blue), 1/4-ring rupture (red) and full-ring rupture (black). The stars show schematically the epicentres for each case, which were calculated from a joint inversion (localisation and MT), note that the epicentres are not located on the fault. The triangles represent seismic stations. b) Normalised maximum amplitudes as a function of epicentral distance. Every MT inversion software uses a point source approach, which tries to fit an amplitude profile similar to the blue line, to the data of our curved sources in red and black. Therefore, proximal stations force the software to overestimate the amplitudes and the magnitude due to the focusing effect inside the caldera. On the other hand, distal stations accurately estimate the magnitude since the dependence of the amplitude decay is similar in this domain. For interpretation of the colour scales in this figure, the reader is referred to the online version of this article.

| Source | $M_o$ (Inverted seismic moment) | $M_o^P$ (Same size planar fault) | $M_o^P/M_o$ |
|---|---|---|---|
| 1/4-ring | $2.79 \times 10^{15}$ Nm | $8.17 \times 10^{15}$ Nm | 2.93 |
| 1/2-ring | $4.35 \times 10^{15}$ Nm | $1.60 \times 10^{16}$ Nm | 3.68 |
| 3/4-ring | $3.16 \times 10^{15}$ Nm | $2.45 \times 10^{16}$ Nm | 7.75 |
| full-ring | $3.37 \times 10^{15}$ Nm | $3.27 \times 10^{16}$ Nm | 9.7 |

Table 2: Seismic moment calculated for different arc length ruptures, the seismic moment for the analogue planar fault and their correction coefficient used to calculate the apparent seismic moment.

after modelling extensively different cases of ring ruptures, we can test the results obtained using different seismic networks and evaluate whether they are suitable for the analysis or they lead to a completely wrong interpretation of the modelled processes.

### *4.1. MT calculations and network configuration*

The ambiguity in the MT results and seismic moment estimations obtained with different network configurations need to be considered and acknowledged. For small earthquakes, for which the point source approximation is valid, we obtain well-constrained MT solutions when the focal sphere of the event is sufficiently covered, Lanza and Waite (2018) indicates that the ideal number

of well-distributed seismic stations is 8. For example, earthquakes at Bárðarbunga are shallow, thus, distant seismic networks do not span the focal sphere adequately. We showed in Fig. 1a and b that the IMO network correctly spans the azimuthal angles, but coverage of the take-off angles is limited, spanning only values around 90°. Thus, the lack of seismic stations in the proximity of the epicentre affects the MT calculation, providing biased results. On the other hand, the ideal network sufficiently covers the focal sphere (Fig. 1c), providing results that can be further analysed. In addition, the inversion software returns a variety of solutions depending on the network considered. Although, they all show a very good fit to the data (Fig. 3) we select as the reliable result the one returned for the ideal network, since it supports the solution provided by Ekström (1994) for partial-ring ruptures. The good match for different sources returned was previously reported by Sindija and Neuberg (2019), who studied the performance of MT inversions for different network configurations and sources at Montserrat, West Indies. In many cases, their results fit the data but failed to retrieve the moment tensor components, hence, we suggest that a good match between input seismograms and synthetics returned from the inversion is not necessarily an indicator of the quality of the inversion.

Complexities during the inversion process arise when the events are shallow compared to the wavelength of radiation. The focal mechanisms for each point source show dip-slip faulting, which according to Kanamori and Given (1981) present intrinsic uncertainties when the MT inversion is performed. In these cases the seismic moment and the dip angle of the fault are poorly constrained due to the lack of radiation produced by the components $M_{xz}$ and $M_{yz}$, only the factor $M_o \sin(2\delta)$ can be accurately calculated (Tsai et al., 2011). Despite the dip-slip nature of the individual sources, the superposition of all contributions is represented mainly by the diagonal of the MT (ISO + CLVD components). Thus, shear components are small compared to the diagonal values, as it is shown for the DC percentages ranging from 8% to 15% for 1/4-ring ruptures in Table 1. Although this effect is intrinsic for MT inversions of shallow earthquakes, in our case, their effect is minimal.

An alternative method to our point source MT inversion is the multiple moment tensor inversion (Tsai et al., 2005) which allows us to calculate the real source parameters of every section on the curved source, which can provide an incredibly detailed description. However, by applying the corrections calculated here, we use a simple method that can account for the destructive interference observed. Furthermore, for the application to Bárðarbunga case, our goal is to calculate the cumulative seismic moment, therefore, only the overall value of the seismic moment is needed, not individual sections.

An important limitation of our modelling is the oversimplification of our elastic medium as a half-space with constant velocity, this means that ray paths are straight lines, i.e. no refraction occurs. In this situation, the rays radiated downwards cannot reach the surface, thus, that information is lost. In real seismic applications, velocity structures produce refraction of waves and we can completely cover the focal sphere, obtaining better-constrained results. More work has to be done considering these propagation effects, but they are beyond the scope of this study.

### *4.2. Magnitude estimation and earthquake location*

Another aspect which affects the MT inversion is the size of the fault and its proximity to seismic stations, for magnitude estimation, the point source approximation must be valid. The size of the rupture must be very small compared to the distance of observation, assuming long wavelengths. Geometrically, the point source location that minimises the misfit of a full-ring rupture is its centre, even though no fault is located there (Fig. 4a). For small conduit-size ring faults, the location is accurate since the horizontal misfit is bigger than the diameter $D \sim 40$ m of the ring. On the other

hand, for caldera-size rings, the point source location is several kilometres away from the actual fault, this produces an artefact in the source parameter estimations. In some extreme cases, the amplitudes can increase by a large amount with distance, and they are not correlated with the radiation patterns or the geometrical spreading, e.g. the black profile in Fig. 4b.

In Fig. 4b, we show the maximum normalised amplitudes produced by a 1/4-ring fault at different distances, by a full-ring rupture (black line) and by a DC point source (blue line). At small epicentral distances, the trend of the amplitude profiles look extremely different, let alone the actual amplitudes. Every MT inversion software is based on a point source approach, regardless of the calculation algorithm, they minimise the misfit between the seismograms and the wavefield produced by the source model. The forward model produced by the MT solution shows a point source amplitude profile (such as the blue line), thus, this profile' shape is used to interpret the data generated by 1/4-ring and full-ring ruptures, which show focusing effect, i.e. profile showing larger amplitudes at proximal stations. Therefore, in order to minimise the misfit in the estimation, the software provides a result one order of magnitude larger than for distal stations (Table 1), i.e. the software inversion systematically overestimates the $M_o$ to fit the amplitudes observed. For distal stations, the decay looks very similar for a point source and a 1/4-ring rupture and eventually for a full-ring rupture at longer distances. Hence, the effect of the fault curvature is reduced at larger distances and the point source approximation retrieves a seismic moment that can be further analysed. This implies that the application of the correction factor still relies on the point source approach, which is valid at long distances. In this way, the local focusing effect at proximal stations is avoided.

In contrast to the result for MT inversion, where proximal stations performed better, seismic moment estimations are better constrained when we use distal stations. This leads to the obvious and simple conclusion that an adequate analysis of moment tensors together with a correct determination of seismic moments which considers complex fault ruptures can only be achieved with sufficiently dense seismic networks that cover a wide area.

### *4.3. Cumulative seismic moment at Bárðarbunga*

The trapdoor caldera collapse at Bárðarbunga produced a maximum subsidence of 65 m at the centre of the caldera (Gudmundsson et al., 2016). Even though the seismicity is concentrated at the north-northwest segment and at the southern segment, Parks et al. (2017) calculated slip around the whole ring structure obtaining an average value of 40 m. Previous studies claimed that the caldera collapse happened mainly aseismically (Riel et al., 2015), due to the difference of more than two orders of magnitude between the smaller seismic moment $M_o$ and the geodetic moment $M_o^{(g)}$ (Riel et al., 2015; Gudmundsson et al., 2016; Ágústsdóttir et al., 2019). However, seismicity is assumed to be planar in all previous studies, which is a good approximation when the rupture area is small compared to the size of the caldera. In contrast, for bigger rupture areas, the curvature of the fault affects the radiation patterns and the seismic moment is always underestimated (Contreras-Arratia and Neuberg, 2019).

Gudmundsson et al. (2016) reported the cumulative seismic moment for the caldera collapse as $5.07 \times 10^{18}$ Nm. We correct this value assuming that partial ring rupture occurs over all the extent of the perimeter (1/4-, 1/2, 3/4-, full-ring ruptures), with a mean rupture arc of around 90°. Therefore, we propose the apparent seismic moment to be $2.9 \times 5.07 \times 10^{18}$ Nm $= 1.5 \times 10^{19}$ Nm. As mentioned above, Gudmundsson et al. (2016) calculated the geodetic moment in the range of $4 \times 10^{19}$ Nm to $4 \times 10^{20}$ Nm depending on different values of rigidity $\mu$. For our synthetic experiments we use $\mu = 10$ GPa which leads to a value of $2 \times 10^{20}$ Nm, which we use as an upper

bound. The vertical extent of the fault needs to be reduced from 12 km to 6 km (Ágústsdóttir et al., 2019) and the slip from 60 m to 40 m (Parks et al., 2017). With all these corrections applied we obtain a geodetic moment ranging from $1.4 \times 10^{19}$ Nm to $6.67 \times 10^{19}$ Nm, which is now in the same order of magnitude as the seismic moment. Furthermore, Heap et al. (2020) have proposed a method to rescale elastic moduli in volcanic environments, e.g. the rigidity is estimated to be 2.1 GPa, which is approximately the lower bound for seismic moment proposed by Gudmundsson et al. (2016). Therefore, we postulate that the seismic and geodetic moments match for smaller and more realistic elastic moduli in volcanic settings. However, for larger rigidity values of intact rock, the geodetic moment is $4 - 5$ times larger than the total seismic moment during the caldera collapse.

If we consider the upper bound, the discrepancy between the geodetic (larger) and the seismic (smaller) moments can be explained by slow earthquakes (Brooks et al., 2006) on lubricated faults (Brodsky and Kanamori, 2001), or fault creeping that produce a tremor-like seismic signal (Rubin et al., 1999). Here we propose that considering only big events $M_w > 4$ at the rim of the caldera, the cumulative seismic moment can be corrected to obtain a larger value, now in the same order of magnitude than the geodetic moment.

## 5. Conclusions

We proved that the direct application of planar fault theory is not appropriate for curved fault seismic sources. However, we can identify clues to conclude that curved sources are acting, such as a moment tensor showing a combination of an isotropic and compensated linear vector dipole.

Moreover, the network configuration is crucial to obtain reliable results. In order to obtain a good representation of the moment tensor, proximal stations are needed. In addition, distal stations are needed for a good seismic moment estimation. Hence, we need a sufficiently good seismic network with stations covering a wide area around the volcano.

Moment tensor results for different kind of ruptures in a caldera-size ring-fault show a deviatoric tensor which is dominated by a compensated linear vector dipole component, however, the isotropic component is the most important, as it is shown in the lune plots in Fig. 2c. The deviatoric tensor shows sub-vertical pressure axes, which supports the conclusion by Ágústsdóttir et al. (2019) of normal faults acting, and give insight that the Bárðarbunga caldera is in stage 4 of evolution according to the model of Acocella (2007).

Our modelling shows that the seismic moment estimation using a point source approach underestimates the magnitude of the earthquakes, which needs to be corrected in order to account for the real rupture area. This correction estimates a seismic moment that matches the geodetic moment for realistic rigidity values. However, for intact rock properties the discrepancy can be up to a factor of 5. This contrast previous estimations that show a seismic moment of around 1% to 10% of the geodetic moment, showing a closer match between these energy estimates of the same process.

We prove that a ring-fault conceptual model can be successfully used to explain seismicity in caldera-size ring-faults. It needs to be carefully applied together with forward modelling in order to exploit its full potential. Future work could also address, the real shape of rims instead of a perfect ring and a stratified media to better constrain the MT solution with real data.

## 6. Acknowledgements

This work was undertaken on ARC4, part of the High Performance Computing facilities at the University of Leeds, UK. RCA is funded ANID Chile through its scholarship program Becas Chile (72170194) and the University of Leeds. JN is partially funded by the Centre for the Observation and Modelling of Earthquakes, Volcanoes and Tectonics (COMET NE/J01978X/1). We also thank the reviewers, for their constructive comments that helped us to improve our manuscript.

## References

Acocella, V., 2007. Understanding caldera structure and development: An overview of analogue models compared to natural calderas. Earth-Science Reviews 85, 125–160.

Ágústsdóttir, T., Winder, T., Woods, J., White, R.S., Greenfield, T., Brandsdóttir, B., 2019. Intense seismicity during the 2014–2015 bárðarbunga-holuhraun rifting event, iceland, reveals the nature of dike-induced earthquakes and caldera collapse mechanisms. Journal of Geophysical Research: Solid Earth 124, 8331–8357.

Aki, K., Richards, P.G., 2002. Quantitative seismology. University Science Books, Sausalito, California. 700pp.

Brodsky, E.E., Kanamori, H., 2001. Elastohydrodynamic lubrication of faults. Journal of Geophysical Research: Solid Earth 106, 16357–16374.

Brooks, B.A., Foster, J.H., Bevis, M., Frazer, L.N., Wolfe, C.J., Behn, M., 2006. Periodic slow earthquakes on the flank of kīlauea volcano, hawai'i. Earth and Planetary Science Letters 246, 207–216.

Cesca, S., Heimann, S., Stammler, K., Dahm, T., 2010. Automated procedure for point and kinematic source inversion at regional distances. Journal of Geophysical Research: Solid Earth 115.

Contreras-Arratia, R., Neuberg, J.W., 2019. Complex seismic sources in volcanic environments: Radiation modelling and moment tensor inversions. Journal of Volcanology and Geothermal Research 381, 262–272.

Ekström, G., 1994. Anomalous earthquakes on volcano ring-fault structures. Earth and Planetary Science Letters 128, 707–712.

Gudmundsson, M.T., Högnadóttir, T., 2007. Volcanic systems and calderas in the vatnajökull region, central iceland: Constraints on crustal structure from gravity data. Journal of Geodynamics 43, 153–169.

Gudmundsson, M.T., Jónsdóttir, K., Hooper, A., Holohan, E.P., Halldórsson, S.A., Ófeigsson, B.G., Cesca, S., Vogfjörd, K.S., Sigmundsson, F., Högnadóttir, T., et al., 2016. Gradual caldera collapse at bárdarbunga volcano, iceland, regulated by lateral magma outflow. Science 353, aaf8988.

Heap, M.J., Villeneuve, M., Albino, F., Farquharson, J.I., Brothelande, E., Amelung, F., Got, J.L., Baud, P., 2020. Towards more realistic values of elastic moduli for volcano modelling. Journal of Volcanology and Geothermal Research 390, 106684.

Heimann, S., Vasyura-Bathke, H., Sudhaus, H., Isken, M.P., Kriegerowski, M., Steinberg, A., Dahm, T., 2019. A python framework for efficient use of pre-computed green's functions in seismological and other physical forward and inverse source problems. Solid Earth 10, 1921–1935.

Kanamori, H., Given, J.W., 1981. Use of long-period surface waves for rapid determination of earthquake-source parameters. Physics of the Earth and Planetary interiors 27, 8–31.

Lanza, F., Waite, G.P., 2018. A nonlinear approach to assess network performance for moment-tensor studies of long-period signals in volcanic settings. Geophysical Journal International 215, 1352–1367.

Nettles, M., Ekström, G., 1998. Faulting mechanism of anomalous earthquakes near bárdarbunga volcano, iceland. Journal of Geophysical Research: Solid Earth 103, 17973–17983.

Parks, M.M., Heimisson, E.R., Sigmundsson, F., Hooper, A., Vogfjörd, K.S., Árnadóttir, T., Ófeigsson, B., Hreinsdóttir, S., Hjartardóttir, Á.R., Einarsson, P., et al., 2017. Evolution of deformation and stress changes during the caldera collapse and dyking at bárdarbunga, 2014–2015: Implication for triggering of seismicity at nearby tungnafellsjökull volcano. Earth and Planetary Science Letters 462, 212–223.

Riel, B., Milillo, P., Simons, M., Lundgren, P., Kanamori, H., Samsonov, S., 2015. The collapse of bárðarbunga caldera, iceland. Geophysical Journal International 202, 446–453.

Roche, O., Druitt, T., Merle, O., 2000. Experimental study of caldera formation. Journal of Geophysical Research: Solid Earth 105, 395–416.

Rodriguez Cardozo, F., Hjorleifsdottir, V., Jonsdottir, K., Geirsson, H., Iglesias, A., 2018. New insights about bárðarbunga's seismic sources during and after the 2014-2015 caldera collapse events, in: AGU Fall Meeting Abstracts.

Rubin, A.M., Gillard, D., Got, J.L., 1999. Streaks of microearthquakes along creeping faults. Nature 400, 635.

Shuler, A., Ekström, G., 2009. Anomalous earthquakes associated with nyiragongo volcano: Observations and potential mechanisms. Journal of Volcanology and Geothermal Research 181, 219–230.

Shuler, A., Ekström, G., Nettles, M., 2013a. Physical mechanisms for vertical-clvd earthquakes at active volcanoes. Journal of Geophysical Research: Solid Earth 118, 1569–1586.

Shuler, A., Nettles, M., Ekström, G., 2013b. Global observation of vertical-clvd earthquakes at active volcanoes. Journal of Geophysical Research: Solid Earth 118, 138–164.

Sindija, D., Neuberg, J., 2019. The effect of seismic network geometry on moment tensor inversions., in: Geophysical Research Abstracts.

Tape, W., Tape, C., 2012. A geometric setting for moment tensors. Geophysical Journal International 190, 476–498.

Tkalčić, H., Dreger, D.S., Foulger, G.R., Julian, B.R., 2009. The puzzle of the 1996 bárdarbunga, iceland, earthquake: No volumetric component in the source mechanism. Bulletin of the Seismological Society of America 99, 3077–3085.

Tromp, J., Komatitsch, D., Liu, Q., 2008. Spectral-element and adjoint methods in seismology. Communications in Computational Physics 3, 1–32.

Tsai, V.C., Hayes, G.P., Duputel, Z., 2011. Constraints on the long-period moment-dip tradeoff for the tohoku earthquake. Geophysical research letters 38.

Tsai, V.C., Nettles, M., Ekström, G., Dziewonski, A.M., 2005. Multiple cmt source analysis of the 2004 sumatra earthquake. Geophysical Research Letters 32.

Wang, R., 1999. A simple orthonormalization method for stable and efficient computation of green's functions. Bulletin of the Seismological Society of America 89, 733–741.